Journal of Magnetic Resonance Open 14–15 (2023) 100088

Contents lists available at ScienceDirect

Journal of Magnetic Resonance Open

journal homepage: www.sciencedirect.com/journal/journal-of-magnetic-resonance-open

# Solid state NMR characterization of $NaNbO_3$ and $LiNbO_3$ nanoparticles obtained by microwave-assisted combustion

Guilherme O. Siqueira [a], Geraldo M. de Lima [b], Francielle C. Araújo [a], Fabrício V. de Andrade [a], Tiago B. Moraes [c,*], Marcos de Oliveira Jr. [d,*]

[a] Instituto de Engenharias Integradas (IEI), Universidade Federal de Itajubá (UNIFEI), Rua Irmã Ivone Drumond, 200, Itabira, MG, CEP 35903-087, Brazil
[b] Departamento de Química, Universidade Federal de Minas Gerais (UFMG), Avenida Antônio Carlos 6627, Belo Horizonte MG, CEP 31270-901, Brazil
[c] Departamento de Engenharia de Biossistemas, Universidade de São Paulo (USP), Avenida Páduas Dias, 11, Piracicaba, SP, CEP 13418-900, Brazil
[d] Instituto de Física de São Carlos, Universidade de São Paulo (USP), PO Box 369, São Carlos, SP, 13560-970, Brazil

ARTICLE INFO

*Keywords:*
Niobates
Nanoparticles
Structure
Photocatalysis

ABSTRACT

Nanoparticles of $LiNbO_3$ and $NaNbO_3$ were obtained for the first time by microwave-assisted combustion. Preliminary experiments reveal that the synthetic conditions influence their microstructure and optoelectronic features. Therefore, there is a need for performing the structural characterization of these materials, obtained by this new route. In the case of $NaNbO_3$, there are two polimorphs which are stable at room temperature, space groups $P2_1ma$ and Pbma. Powder x-Ray diffraction experiments were not capable to identify the crystalline phases present in the nanoparticles. Therefore, we have performed a detailed structural characterization of the nanoparticles by 1D and 2D solid state $^{23}Na$ and $^{93}Nb$ Nuclear Magnetic Resonance (NMR) techniques. $^{23}Na$ results reveal the presence of both phases, Pbma and $P2_1ma$, for samples prepared using $NaNO_3$ precursor in a 1:1 Na:Nb ratio or NaCl in excess. On the other hand, the $P2_1ma$ polymorph could be isolated in the synthesis using NaCl salt in 1:1 Na:Nb ratio. On the other hand, $LiNbO_3$ nanoparticles display the usual rhombohedral structure R3c. $^{7}Li$ MAS NMR results reveal the presence of two types of Li species, with distinct dynamics. Highly mobile $Li^+$ ions are found at the surface of the nanoparticles, while bulk $Li^+$ show restricted movement. Finally, as a proof of principle, the photocatalytic activity of these niobates was tested for the degradation of methylene blue dye, a common organic-water contaminant.

## 1. Introduction

Alkali niobate materials display growing technological importance due to their interesting properties. For example, $NaNbO_3$ has high dielectric permittivity, ferroelectric and piezoelectric properties, adequate for use in some devices, such as dielectric capacitors with high energy storage density and power density piezoelectric actuators, sensors and transducers, ferroelectric memories and electromechanical systems [1–4]. On the other hand, $LiNbO_3$ has interesting electrical-mechanic properties, high non-linear electro-optic coefficients, natural birefringence, large refractive index and wide transparency wavelength. These features make these materials good candidates for applications such as optical memory, waveguide modular, high-speed modulator, frequency conversion, second harmonic generation, and surface acoustic wave among others [5–8]. These materials might substitute others that contain heavy metals in the construction of healthy and environmentally safe devices.

The environmental applications of lithium or sodium niobates are being investigated lately. Due to their chemical stability, facile preparation and because they are semiconductors with a large bandgap generating high energy electron/hole pairs, suitable for the degradation of organic pollutants. Recently, $NaNbO_3$ nanorods modified graphitic carbon nitride was applied to degrade ofloxacin in water solution under simulated solar radiation, demonstrating high efficiency [9] $LiNbO_3$ ceramic-supported Ag nanoparticles were tested in the photodegradation of organic dye induced by visible light, showing promising results [10].

There are several approaches reported in the literature for syntheses of lithium and sodium niobates. Among them, stands the hydrothermal synthesis with microwave-assisted [2,9,11,12] and solid-state reactions

*Abbreviations:* NMR, Nuclear Magnetic Resonance; XRD, X-ray diffraction; HRTEM, High-Resolution Transmission Electron Microscopy; MB, Methylene Blue dye.

* Corresponding authors.
*E-mail addresses:* tiago.moraes@usp.br (T.B. Moraes), mjunior@ifsc.usp.br (M. de Oliveira).

https://doi.org/10.1016/j.jmro.2022.100088

Available online 17 December 2022

[13,14]. For example, $NaNbO_3$ has been synthesized by designed Surface Ligand-Assisted Localized Crystallization (SLALC) [11], while $LiNbO_3$ was obtained by surfactant-assisted solution-phase method [15], non-aqueous sol-gel reaction [16] or by the molten salt procedure [17].

Combustion synthesis is an attractive chemical industrial process since it requires modest equipment, low energy and produces a low amount of residues [18]. The method consists of mixing two solid reactants, one is the comburent, an oxidizing agent, usually a nitrate salt, and the other is the fuel, a reducing agent, usually an organic compound. The system receives external heat only up to the ignition point, at which the process is self-sustained by the heat released by the strong exotherm reaction and reaches a high temperature in a very short time. The high volume of gas quickly released by the reaction prevents the agglomeration and the growth of the oxide particles produced and the high-temperature guarantee a low density of defects in the crystalline structure [19]. The use of microwave energy makes it possible to reach the ignition point much faster than other heating methods [18]. Several materials were produced by combustion synthesis, some were recently published: $Y_3Fe_5O_{12}$ [20], $MgAl_2O_4$ [21], MnFeCoNiCu and $(MnFeCoNiCu)_3O_4$ [22].

In this work, nanoparticles of $NaNbO_3$ or $LiNbO_3$ were produced using this synthetic approach. To the best of our knowledge, it is the first time that this synthetic method is employed in the preparation of alkaline metal niobates. Due to the novelty of this synthesis approach, the structural characterization of the resulting material is of great importance. In the case of $LiNbO_3$ X-ray powder diffraction (XRPD) provide an unambiguous determination of the crystalline structure. On the other hand, for the $NaNbO_3$ compound there is a high degree of superposition for the difractograms of both polymorphs which are stable at room temperature, space groups $P2_1ma$ and Pbma [23]. For the determination of the crystalline phases present in the structure, solid state $^{23}Na$ NMR is a very well-suited technique. According to the study of Johnston et al. [23], $^{23}Na$ isotropic chemical shifts and quadrupolar coupling parameters are different for distinct polymorphs. When more than one polymorph is present in the structure, bidimentional multiple-quantum MAS (MQMAS) correlation spectroscopy, combined with spectral simulations, can be used to provide structural information. Additionally, the quantitative character of the NMR technique allows for the quantification of the relative concentration of each phase in the sample. Finally, $^{23}Nb$ NMR provides complementary information about the Nb coordination environment, while $^{7}Li$ NMR can reveal the presence of highly mobile $Li^+$ions, which cannot be detected by powder X-ray Diffraction (XRD) [24].

Finally, complementary information about microstructure and optical properties is provided by a combination of electron microscopy and optical spectroscopy. Also, it is well known that niobate nanoparticles are efficient for the photocatalytic degradation of organic molecules in water [9,10,25-27]. Therefore, the photocatalytic activity of the $LiNbO_3$ and $NaNbO_3$ compounds obtained in this work was tested.

### 1.1. Preparation of samples

Nanoparticles of alkaline niobates were obtained by microwave-assisted combustion. Ammonium niobium oxalate ($NH_4[NbO(C_2O_4)_2(H_2O)].H_2O$) and alkaline salt ($NaNO_3$, NaCl and $LiNO_3$) were used as precursor reagents and source of the cations. Urea $\{(H_3N)_2C{=}O\}$ was employed as a reducing agent (fuel) and ammonium nitrate ($NH_4NO_3$) as an oxidizing chemical (comburent). The procedure follows the chemical concept of the propellants [28], where the details can be found in the literature [29]. An aqueous solution was prepared with the fuel and comburent, following the elemental stoichiometric coefficient [28]. The combustion reaction was performed in a microwave oven (700 W) operating for 7 min at 2.45 GHz. The first step was the evaporation of water followed by the heating of the solids to the ignition point, at which a large volume of gaseous products is rapidly eliminated and the product is formed. A summary of the synthesis conditions and the sample codes are shown in Table 1. The yields of the reactions were calculated between 46 and 52%.

### 1.2. Characterization

The powder XRD patterns were collected in a Shimadzu Diffractometer model XRD-7000. The X-ray set to a current of 30 mA and a voltage of 30 kV, with the CuKα radiation, at a scan rate of $4^\circ$ 2θ.min$^{-1}$, with 2θ from 15 to $70^\circ$ The absorption spectra were obtained with a UV–Vis Shimadzu spectrophotometer model UV 2700. Scanning Electron Microscopy (SEM) was used to investigate the morphology of the obtained materials. The images were obtained in a VEGA3 TESCAN equipment. High-resolution transmission electron microscopy (HRTEM) images were obtained using a Tecnai G2–20 SuperTwin FEI microscope at 200 kV. For SEM measurements, samples were re-dispersed in acetone in an ultrasonic bath, with the aid of a Pasteur pipette, the formed suspension being subsequently dripped on heated aluminum support. The same sample preparation was used for HRTEM but, instead of aluminum support, a holey carbon film on a 200 mesh copper grid was used.

Solid-state NMR spectra were measured on a Bruker Avance Neo spectrometer operating at 14.1 T (600 MHz for 1H Larmor frequency) equipped with a Bruker HX 1.3 mm probe. Spectra were obtained from single-pulse experiments, using short excitation pulses of 1.0 μs (corresponding to flip-angles below $30^\circ$). Additional experimental parameters are given in Table 2. For $^{93}Nb$ NMR spectra, rolling baseline artefacts visible in the single-pulse spectra were removed by spline fitting. $^{23}Na$ Triple-quantum MAS NMR (MQMAS) spectra were measured using the three-pulse z-filtering sequence [30], using hard excitation and reconversion pulses of 4.0 μs and 1.5 μs length and soft detection pulses of 10.5 μs length. Spectral simulations were performed using the Simpson package [31]. In order to obtain reliable values for the complete set of parameters involved in the $^{93}Nb$ simulations, they were optimized using genetic algorithm procedures [32]. The method uses the SIMPSON code as a computational kernel and was implemented in MATLAB (MathWorks, Inc.). To simulate the powder spectra, an averaging over the different crystallite orientations was simulated by using a REPULSION (REP) powder angle scheme with 320 crystallite orientations [33]. Convolution with Gaussian functions was applied to the final simulated spectra to reproduce the linewidths observed experimentally. $^{7}Li$, $^{23}Na$ and $^{93}Nb$ resonance frequencies were externally referenced relative respectively to 1 M LiCl (aq) (using solid LiCl, $\delta = -1.1$ ppm, as secondary standard [34]), 1 M NaCl (aq) (using solid NaCl, $\delta = 7.3$ ppm, as secondary standard [23]) and a saturated solution of $NbCl_5$ in acetonitrile.

### 1.3. Photocatalytic activity testing

Photocatalytic tests were conducted by adding about 100 mg of the catalysts, to 30 ml of aqueous solutions of methylene blue dye (MB) (forming two systems), with a concentration equal to 50 ppm, used in the present work as a contaminant model. The systems were placed (one at a time) in a photo-reactor equipped with ultraviolet radiation from two 24 W lamps and a thermostatic system, to guarantee a constant temperature during the experiment. Before switching on the lamp, the

**Table 1**
Summary of synthesis details for the preparation of alkaline niobates nanoparticles. Throughout the text, the samples are referred to the numbers in brackets.

| Sample | Salt | Nb Molar Ratio | Alkali Molar Ratio | Yield /% |
|---|---|---|---|---|
| $LiNbO_3$ (1) | $LiNO_3$ | 1 | 1 | 51.7 |
| $NaNbO_3$ (2) | NaCl | 1 | 1 | 51.4 |
| $NaNbO_3$ (3) | NaCl | 1 | 23* | 46.1 |
| $NaNbO_3$ (4) | $NaNO_3$ | 1 | 1 | 51.9 |

*Excess of alkali salt.

**Table 2**
Experimental parameters used to measure the single-pulse NMR spectra.

| Isotope | MAS (kHz) | Scans performed | Recycle delay (s) |
|---|---|---|---|
| $^{7}$Li | 10.0 | 4 | 5.0 |
| $^{23}$Na | 15.0 | 64 | 15.0 |
| $^{93}$Nb | 40.0 | 20,000 | 0.2 |

reaction system was left in mechanical agitation in the dark for 30 min, which was necessary to reach the adsorption-desorption balance. After this step, the lamp was turned on, and a 1 mL aliquot was removed from the system every 10 min. The concentration of the MB solutions was monitored with UV–vis spectroscopy measurements, using a Spectrophotometer PG Instruments Ltd equipment, model T-80 UV/Vis. For this purpose, absorbance measurements were made, using $\lambda_{max}$ as a parameter of the dye (664 nm). Before UV–vis measurements, the samples were centrifuged at 4800 rpm for 10 min in a centrifuge Quimis model Q222T1, to remove the catalyst from the solution. Right after the centrifugation of the samples, 0.8 mL aliquots were removed, transferred to a 5 mL volumetric flask, and the flask volume was then made up with deionized water. This procedure was adopted to avoid large variations in volume in the reaction system and to keep the distance from the light source to the solution, with the least possible variation. The UV–vis measurements were used to investigate the kinetics of the catalytic process. Finally, the kinetics of the reactions were investigated in an acidic (pH around 1), and alkaline (pH around 12), as well medium. For the pH adjustment, were used solutions of HCl and NaOH at 1 M.

## 2. Results and discussion

### 2.1. Structure and morphology

Fig. 1 shows the powder XRD diffractograms for the obtained samples. The XRD pattern for sample (1) shows only reflections corresponding to rhombohedral $LiNbO_3$ (space group R3c, ICDD 74–2243). Sodium niobate has a perovskite structure and there are various polymorphs with some typical perovskite distortions [23]. The XRD patterns (Fig. 1) of all samples containing $Na^+$ show reflections related to the orthorhombic $NaNbO_3$ phase, related either to space group $P2_1ma$ (ICDD 82–606 [35]) or Pbma (ICDD 33–1270). The diffractogram of these two structures are similar, the difference is only a few low-intensity reflections, about 2% of the main peak (see the subtitle of Fig. 1), which makes them exceedingly difficult to differentiate only by XRD. However, solid-state $^{23}$Na-NMR results are more informative, revealing that the phase $P2_1ma$ is dominant for sample (2), while for (3) and (4) a mixture of both phases, $P2_1ma$ and Pbma, is found. The literature [36,37] shows that the predominance of phases of $NaNbO_3$ depends not only upon temperature, but particle sizes also play an important role, for example, the phase $P2_1ma$ may be stable at room temperature if the particles are submicrometric.

The widths of diffraction reflections are influenced by the microstructure of the materials, size of crystals and crystalline distortions [38]. The reflections shown in the diffractograms of all samples are very wide, indicating that the crystals of these samples are small and/or the density of defects is not negligible. The peaks full width at half maximum (FWHM) are different among the samples. The peak at 32.30° 2θ for samples (2), (3) and (4) displays FWHM of 2θ from 0.48 to 0.52°, while for sample (1) the peak of 2θ at 32.60° displays an FWHM of 2θ = 0.40° The FWHM of the instrument is estimated at 0.37° at this angle. These results indicate that the microstructure of these materials depends on the stoichiometry and the conditions used in the synthesis. The chart inserted in Fig. 1 is the Williamson-Hall plot, FWHM.cos(θ) vs 4.sin(θ), for the four samples using the main reflections of the diffractograms [39]. The slope of linear regression of the data is the mean microstrain (ε) and the intercept is $K{\cdot}\lambda/\tau$, where λ is the wavelength of the radiation, K is the Scherrer constant and τ is the mean crystal size. A measure of Si standard was used to subtract the instrumental FWHM. The result of the microstructure is shown in Table 3. The points for sample 1 have not a linear trend and they have a negative slope. In this case, the microstructure calculated by this method is not accurate and the results are not considered here. The microstrain is not negligible for these samples, ranging between 0.08% for Sample (2) and 0.47% for Sample (4). The τ calculated by this method is a volume-weighted average of the size distribution of all crystals illuminated by the incident x-ray beam on a diffractometer, so, this parameter is affected by the distribution but cannot be used to evaluate the breadth of the size distribution. The τ for the samples of sodium range between 29 nm for sample (3) and 33 nm for sample (4). These results follow the same trend found by microscopy and UV–Vis methods.

Electron microscopic experiments were used to characterize the morphology of the niobates. The images of the sample (2) are shown in Fig. 2, with letters a, b, c and d. Scanning electron microscopy (SEM) experiments (Fig. 2a) revealed irregular agglomerates on the micrometer scale, with some particles with sizes near 90 nm. Smaller particles, with diameters of 4 nm can also be identified in the high-resolution transmission electron microscopy (HRTEM) image (Fig. 2b). Fast Fourier transform (FFT) reveals three families of lattice planes in the orthorhombic phase, identified as (101), (200) and (202). More structural details of the sample were displayed by selected area electron diffraction (SAED) experiments (Fig. 2c). Eighth diffraction reflections of the orthorhombic structure were identified in the radial profile of the obtained SAED image (Fig. 2d): (101), (200), (202), (141), (321), (400), (420) and (501).

TEM images of the sample (3) (Fig. 2e) show particles with a size between 4 and 100 nm, but with a predominance of smaller particles. On the other hand, particles up to 700 nm were found in the TEM images of the sample (4) (Fig. 2f), although particles with 4 nm were found in this sample, larger particles are present in greater quantity. FFT processing of HRTEM images of these two samples reveals interplanar distances (Miller index) of 0.39(1 0 1), 0.28(2 0 0) and 0.20nm(2 0 2), all planes are of the orthorhombic structure of sodium niobate.

For Sample (1) (Fig. 2f), the images of microscopy show particles with sizes from 4 to 500 nm, with the predominance of large particles. The microscopy results confirm the influence of the synthetic conditions on the microstructure of niobates: an excess of alkaline salt can inhibit particle growth, and the alkaline salt counter-ion drastically changes the particle size, in this case, chloride produces particles smaller than the nitrate anion.

### 2.2. Optical absorption properties

The electronic structure of a perfect crystalline material is determined by the crystal structure and chemical composition. However, some effects can make changes to the perfect crystal electronic bands. Deformations in the crystal lattice generate Gaussian broadening of the electronic bands. This effect promotes a decrease in the bandgap of a semiconductor and the absorption edge in the absorption spectroscopy is displaced to smaller values of energy. On the other hand, electrostatic potential changes in the crystal promote fluctuations in the bands' edge that cause an exponential tail below the edge of absorption, known as Urbach tail [40]. Crystal defects, e.g. vacancy, dislocation and impurities, can cause both deformation and electrostatic changes and decrease the bandgap. Another important characteristic that can affect the electronic structure is the crystal size. When the radius of the crystals is close to/or smaller than Bohr radius of the material, the quantum confinement effect can be observed, and it increases the bandgap [10] of the semiconductor. All these effects can occur simultaneously in a nanomaterial and the observed bandgap can be bigger or smaller than a perfect crystal depending on which effect is predominant.

Absorption spectroscopy in the ultraviolet and visible regions can be used to study the electronic structure of the semiconductor. These

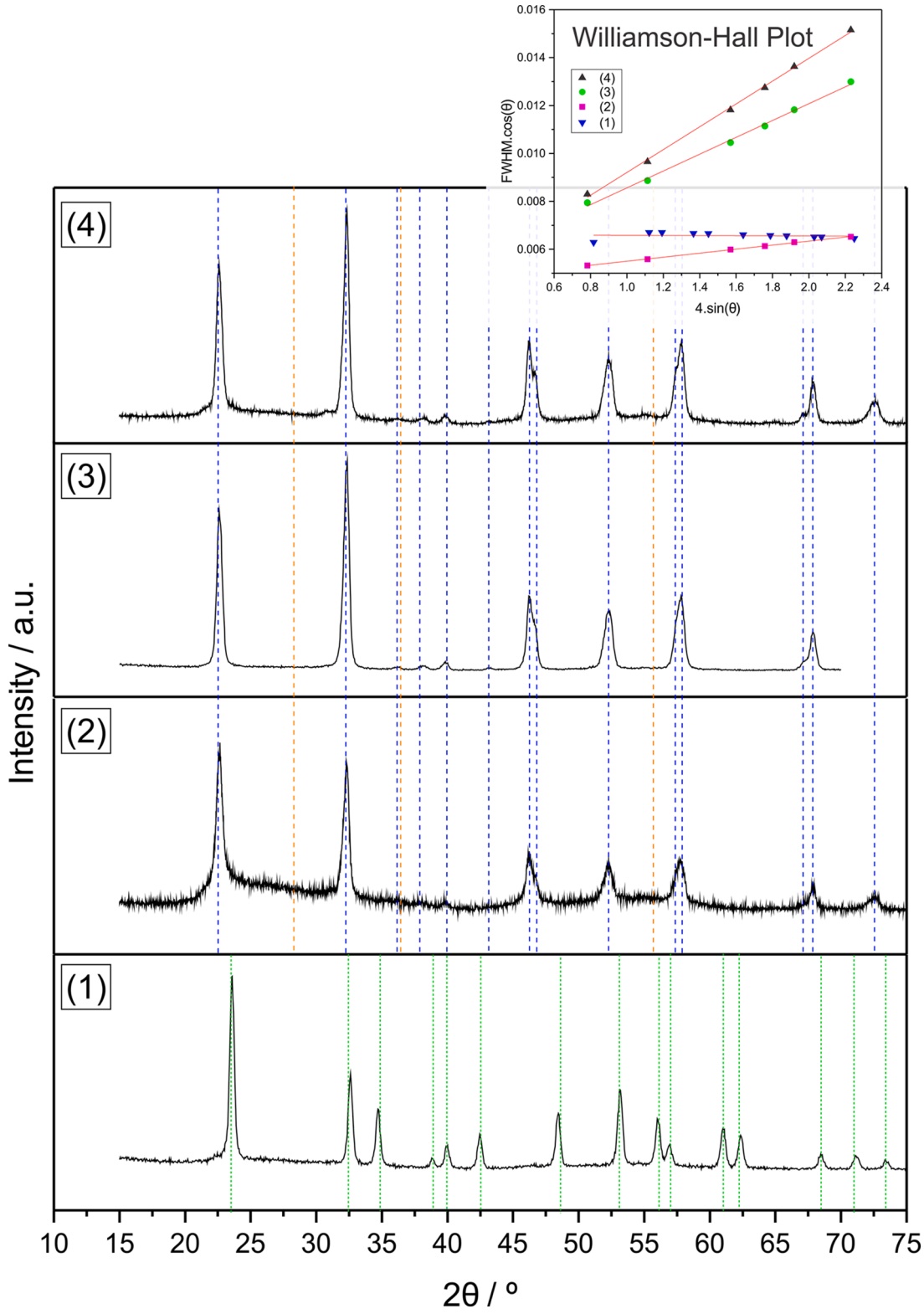


**Fig. 1.** X-ray diffraction results. The reflections of samples (2), (3) and (4) match with an orthorhombic structure (blue vertical lines, $P2_1ma$, ICDD 82–606) and (1) match a rhombohedral structure (green vertical lines, ICDD 74–2243). Orange vertical lines are some low reflections exclusively of orthorhombic Pbma phase (ICDD 33–1270) (2θ|$I/I_{max}$): 28.58|0.009; 36.62|0.012 and 55.16|0.018. The chart inserted is the Williamson-Hall plot.

spectra are shown in Fig. 3 for all samples and the bandgap was calculated by Tauc equation [40]:

$$(\alpha h\nu)^n = A\left(h\nu - E_g\right) \quad (1)$$

where α is absorptivity, h is Plank constant, υ is the frequency of the photon, Eg bandgap energy and A is a constant. It is considered an indirect bandgap for these phases [41,42] and the coefficient in the Tauc equation is taken as 1/2. The inserted graph in Fig. 3 is the Tauc plot and the results are shown in Table 3.

**Table 3**
Results of UV–Vis and Williamson-Hall plot: Bandgap energy (Eg), standard deviation (sd) of bandgap, Urbach Energy (Eu), mean size (τ) and microstrain (ε).

| Sample | Eg (sd*)/ eV | Eu / eV | τ / nm | ε /% |
|---|---|---|---|---|
| LiNbO3 (1) | 3.33 (0.05) | 0.39 | – | – |
| NaNbO3 (2) | 3.18 (0.01) | 0.34 | 31 | 0.08 |
| NaNbO3 (3) | 3.40 (0.03) | 0.34 | 29 | 0.35 |
| NaNbO3 (4) | 3.19 (0.06) | 0.34 | 33 | 0.47 |

* Standard deviation derivate from linear regression.

The bandgap values of the sodium niobates are within the wide range found in the literature for this material, 3.08 - 3.42 eV [42–44]. Sample (3) has the biggest bandgap among the sodium samples, 3.40 eV. For this sample, the quantum confinement effect can be predominant and increase the bandgap compared to samples (2) and (4). This denotes that sample (3) has a smaller crystal size than the other samples. The same conclusion is supported by the XRD and HRTEM results. The salt excess utilized in the synthesis of (3) is expected to impose a physical barrier or physical distance to the reactant molecules, limiting the crystal growth of the oxides produced.

The bandgap for sample (1), 3.33 eV is very close to the value reported in the literature (3.28 eV [41]), suggesting the formation of larger crystals and little influence from the effect of quantum confinement. The lattice distortions effect in this sample stands out, decreasing the bandgap.

The Urbach energies (Eu) were calculated by exponential region of the absorption edge of the spectrum by applying Eq. (2):

$$\alpha = A' e^{\left(\frac{h\nu}{Eu}\right)} \quad (2)$$

where Eu is the Urbach energy and A' is a constant. This energy is associated with Urbach Tails is useful to characterize the degree of defects and how they influence the imperfections in the lattice [45]. Eu from typical crystalline material at room temperature is less than 0.1 eV [46]. For $LiNbO_3$ single crystal it is found in literature at 0.082 eV [47]. The four samples show rather large Urbach energy values (Table 3), higher than 0.34 eV. Nanomaterials often have high Eu in view of their surface defects [48]. The samples containing sodium have very close values of Eu, lower than those found for the lithium niobate, suggesting a higher defect density in the samples containing Li.

### 2.3. Solid state NMR characterization

$^{23}$Na spectra obtained for the sodium-niobates (2), (3), and (4), are shown as black curves in Fig. 4. The $^{23}$Na spectral lineshapes result from the superposition of multiple quadrupolar powder patterns corresponding to distinct Na sites. In order to resolve the observed $^{23}$Na signals, we have acquired a representative bi-dimensional $^{23}$Na MQMAS NMR spectrum for sample (3), shown in Fig. 5a.

The horizontal dimension ($\delta_1$) shows the anisotropic quadrupolar $^{23}$Na powder pattern, while the vertical dimension ($\delta_2$) shows isotropic projections of the spectra, with positions given by a combination of isotropic chemical shift and second-order quadrupolar shift. Three cross-peaks can be easily distinguished in the MQMAS spectrum, with $\delta_1$ shifts near -4.5, -1.8 and 2.0 ppm. From the positions of the MQMAS peaks in both dimensions, information can be obtained about the $^{23}$Na isotropic chemical shifts ($\delta_{iso}$) and second-order quadrupolar coupling effect (SOQE) constant $P_Q = C_Q/(1+\eta^2/3)^{1/2}$, where CQ is the quadrupolar coupling constant and η is the asymmetry parameter of the electric field gradient tensor. Table 4 shows the values of $\delta_{iso}$and PQ obtained from the MQMAS spectra of the sample (3). Fig. 5b shows horizontal projections of the bidimensional spectrum taken for each of the observed $\delta_1$ shifts. Using as an initial guess the $\delta_{iso}$and PQ values obtained from the peak positions in the MQMAS spectrum, each projection could be reproduced by spectral simulations of quadrupolar powder patterns. The first projection (Fig. 5b, top spectrum) could be simulated with two spectral components, corresponding to Na sites which we will call here Na1 and Na4. The second and third horizontal projections (Fig.5b, middle and bottom spectrum respectively) could be simulated with a single component each, corresponding respectively to Na3 and Na2 sites.

Taking as a starting point the approximated simulations of the MQMAS projections, satisfactory simulations of the single-pulse $^{23}$Na MAS spectra could be obtained for all samples. The final parameters for the simulations are shown in Table 4. Besides the sites observed in the MQMAS spectrum, a fifth site (Na5) with minor intensity can be observed in the $^{23}$Na MAS spectra (see inset in Fig. 4. No quadrupolar parameters could be obtained for this site and it is reproduced by Gaussian lineshapes in the spectra of Fig. 4.

Considering the $^{23}$Na spectral lines with major intensity, four Na sites could be observed for samples (3) and (4), indicating the coexistence of different $NaNbO_3$ phases. On the other hand, for sample (2) only two components are observed. Table 4 also shows $^{23}$Na isotropic chemical shifts and quadrupolar coupling constants obtained for $NaNbO_3$ samples with crystalline phases $P2_1ma$ and Pbcm, as reported by Johnston et al. [23]. The parameters obtained for sites 1 and 2 are very close to those reported for the $NaNbO_3$ $P2_1ma$ phase. Therefore, we confirm that sample (2) is in the $P2_1ma$ crystalline structure. For samples (3) and (4) a heterogeneous environment is observed. Besides the $P2_1ma$ phase, a fraction of the sample (~20%) is found in a different crystalline phase. The quadrupolar parameters for site 4 are in close agreement with the Pbcm phase, however, a certain discrepancy is found for site 3. We tentatively attribute sites 2 and 3 to Na in a slightly distorted Pbcm environment. Finally, the peak centered around 9 to 10 ppm (site Na5) comprises about 5% of the overall spectral area. This low-field chemical shift value indicates a cationic character for sodium and we tentatively attribute site Na5 to $Na^+$ ions in defect sites on the surface of the particles.

Fig. 6 shows the single pulse $^7$Li MAS NMR spectrum for sample $LiNbO_3$ (black curves) and the spectral deconvolution into Gauss/Lorentz functions (coloured curves). The parameters of the deconvolution are displayed in Table 5.

The $^7$Li spectrum could be represented by four components, being a broad component represented by a Voigt function (Gauss/Lorentz fraction equal 0.3) centered around -0.9 ppm and three narrow components represented by Lorentzian functions centered around -1.1, -1.2 and -1.5 ppm. The broad component (green curve in Fig. 6) corresponds to Li species with restricted mobility and can be attributed to Li atoms at crystalline domains in the bulk of the material [24,49,50]. On the other hand, the sharp lines at -1.2 and -1.1 ppm correspond to highly mobile Li species (as confirmed by the lack of spinning sidebands, see inset in Fig. 6) at the surface of the material [24,49,50]. The $^7$Li resonance at -1.5 ppm is also probably due to Li in defect sites. This peak shows first-order spinning sidebands with some intensity (see first order spinning sidebands on the inset in Fig. 6), indicating intermediate mobility for these species, i.e., chemical shift anisotropy is not completely averaged out by motion. According to Yao Yu et al. [24], the high Li diffusivity on the surface of $LiNbO_3$ at room temperature is explained by the presence of oxygen vacancies on the surface. They report that the sharp $^7$Li resonance is eliminated after successive annealing of the sample in air.

Fig. 7 shows single pulse $^{93}$Nb MAS NMR spectra measured for the studied compounds (black curves). Although a heterogeneous environment was observed from $^{23}$Na NMR results for samples $NaNbO_3$ (3) and (4) (a probable mixture of crystalline phases $P2_1ma$ and Pbcm), all $^{93}$Nb spectra could be simulated with a single spectral component. Previous results on $NaNbO_3$ polymorphs show that, in principle, it is not possible to distinguish between $P2_1ma$ and Pbcm based on the $^{93}$Nb spectra phases, due to the similarity of the Nb coordination environment in both

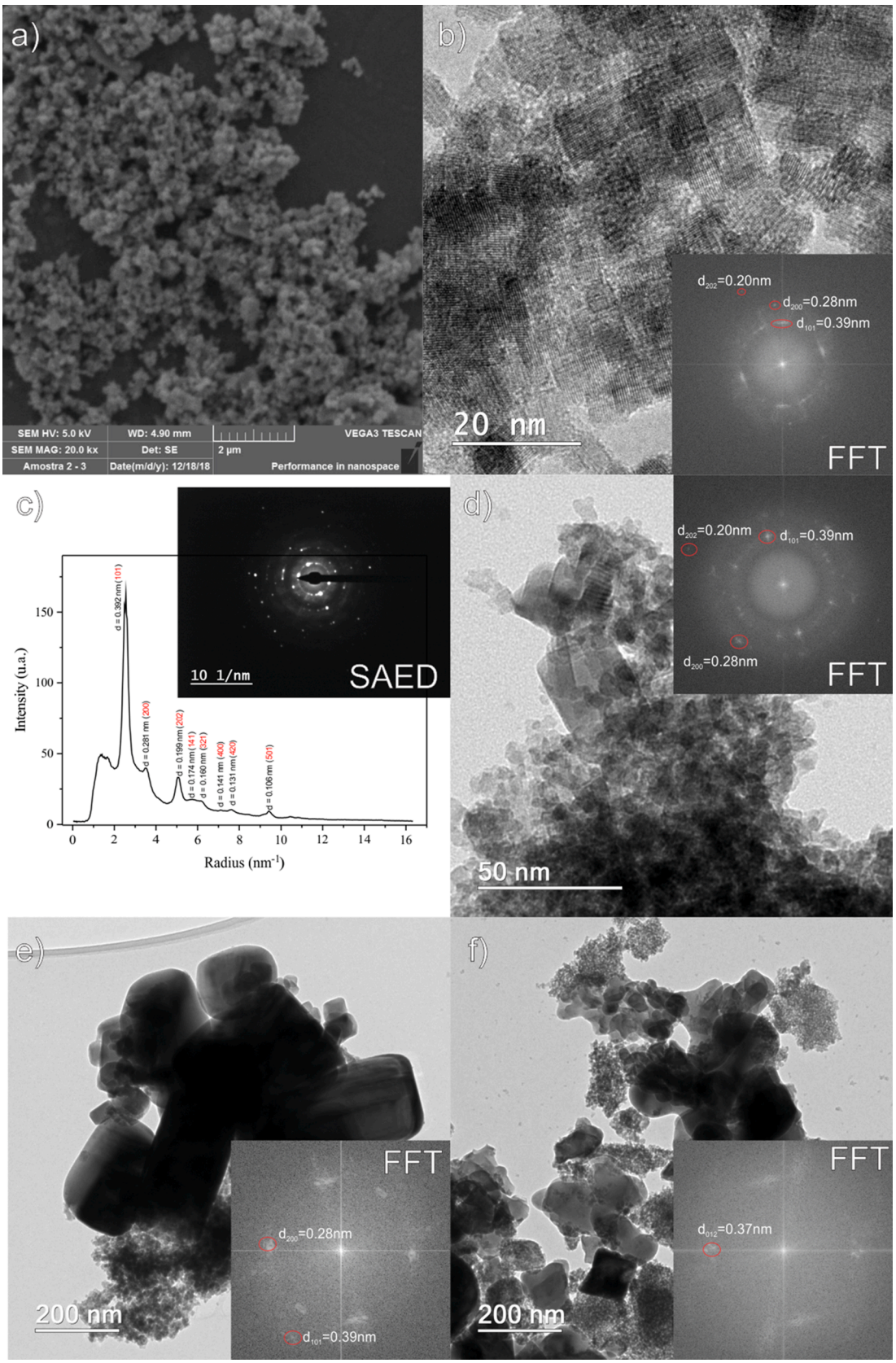


**Fig. 2.** Microscopy results of the sample (2): a) Scan Electron Microscopy (SEM). b) High-Resolution Transmission Electron Microscopy (HRTEM). c) Selected Area Electron Diffraction (SAED) . d) and Radial profile of the SAED with Miller Index of orthorhombic $NaNbO_3$. d) sample (3), e) sample (4) and f) sample (1).

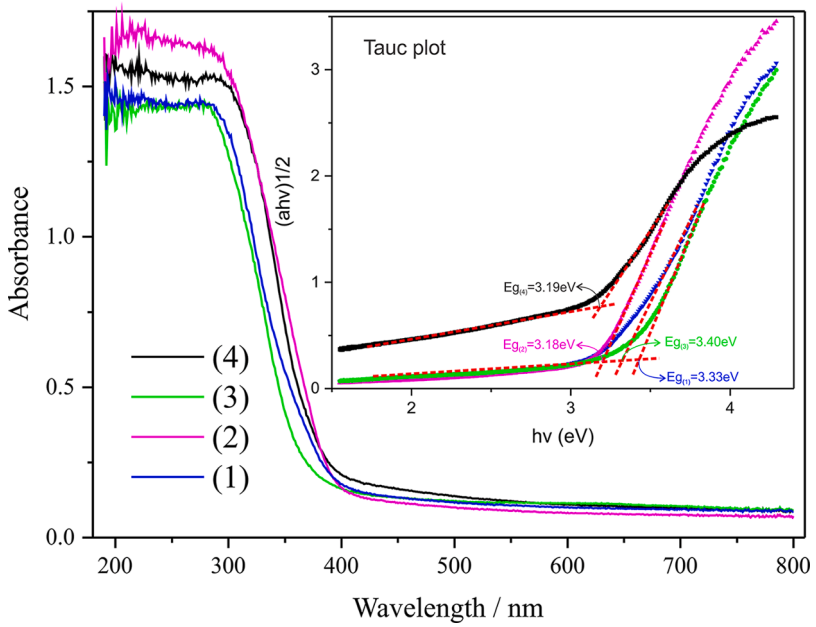


**Fig. 3.** Ultraviolet and visible absorption spectroscopy (UV–Vis) of all samples. The inserted graph is the Tauc plot to calculate the band gap energy (Eg).

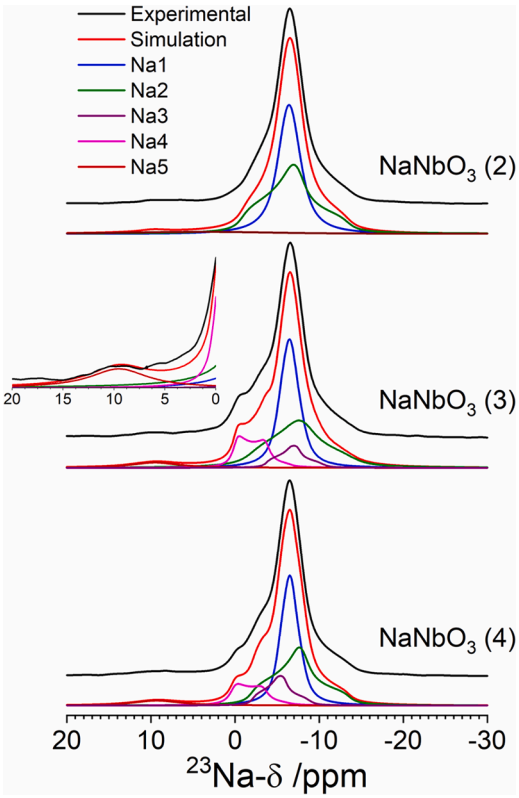


**Fig. 4.** Experimental (black curves) and simulated (coloured curves) $^{23}$Na NMR spectra of the samples **(2)** – **(4)**. Simulations were performed taking as starting guess the spectral parameters obtained from triple quantum MQMAS experiments. The inset shows in detail the region from 0 to 20 ppm for sample $NaNbO_3$ (3), where a minor signal can be observed (Na5).

systems [51]. The simulations are shown as red curves in Fig. 7 and the spectral parameters are shown in Table 6. The simulations consider a system with quadrupolar coupling interaction and chemical shift anisotropy. The simulated spectra were convoluted with a Gaussian function in order to reproduce the linewidth observed experimentally. The width of the Gaussian function (lb) is also shown in Table 6.

The chemical shift anisotropy and asymmetry parameters have a very small effect on the spectral lineshape, therefore, an axial chemical shift interaction was considered aiming to better reproduce the first order spinning sidebands. For all $NaNbO_3$ samples, a rhombic electric field gradient is found for the $^{93}$Nb local environment, with a quadrupolar coupling interaction constant CQ of 21 ± 1 MHz and asymmetry parameter η of 0.6 for samples (2) and (3) and 0.7 for sample (4). The parameters observed by us are in complete agreement with literature data for both Pbcm and $P2_1ma$ phases of $NaNbO_3$ [51], being $^{93}$Nb MAS NMR unable to resolve them. On the other hand, for the $LiNbO_3$ sample, the $^{93}$Nb is found in a nearly axial environment, with $\eta = 0.1$ and CQ = 22 ± 1 MHz. These parameters are in complete agreement with the $LiNbO_3$ trigonal phase [52–55]. Finally, larger broadening parameters were necessary to reproduce $^{93}$Nb NMR spectra for $NaNbO_3$ samples, indicating a larger degree of disorder for these samples, as suggested by XRD data.

### 2.4. Photocatalysis tests

Several works in literature have been reported that lithium and sodium niobates synthesized by other routes have photocatalytic activity. $NaNbO_3$ obtained by hydrothermal route [9] showed photocatalytic activity for degradation of ofloxacin and when obtained by polymeric citrate precursor [26] and by polymer complex method [27] they are able to degrade rhodamine B. On the other hand, $LiNbO_3$ obtained by solid state reaction [10] showed photocatalytic activity for degradation of rhodamine B. Semiconductors with nanoscale particles is an important feature to achieve good results in photocatalysis because the charge transfer step occurs on surface particle. The synthesis method used in this work allows obtaining materials in a single step with low energy consumption with adequate morphology to photocatalysis. Therefore, the photocatalytic methylene blue (MB) degradation test was performed to verify the activity of the samples.

The photocatalytic activity of samples (1) and (2) were tested by adding about 100 mg of the niobates to 30 ml of aqueous solutions and MB in a concentration of 50 ppm. Fig. 8 shows the percentage of MB removal from the solution by alkaline niobates ($LiNbO_3$ (1), and $NaNbO_3$ (2)), at two different pHs (pH 1, Fig. 8a, and pH 12, Fig. 8b), after reaching the adsorption equilibrium. The removal percentage was

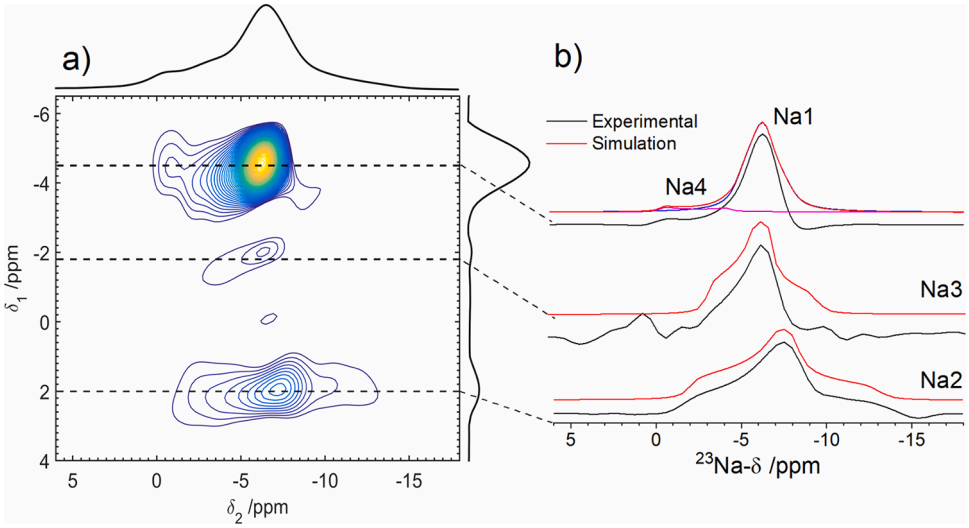


**Fig. 5.** (a) $^{23}$Na triple-quantum MQMAS spectrum for the $NaNbO_3$ sample **(3)**. (b) Horizontal projections of the 2D-MQMAS spectrum taken from the spectral slices with $\delta_1$ shifts near -4.5, -1.8 and 2.0 ppm (black curves). Spectral simulations of the projections are also shown. The simulations consider quadrupolar powder patterns.

**Table 4**
Experimental $^{23}$Na NMR Parameters, $\delta_{iso}$, $P_Q$, $C_Q$, and η, for the studied samples obtained from the single-pulse MAS and MQMAS spectra in Figs. 4 and 5a respectively. Data from the literature are also shown for the $NaNbO_3$ $P2_1ma$ and Pbcm crystalline phases.

| Sample | Na site | 23Na single-pulse MAS spectral simulations | | | | 23Na MQMAS | |
|---|---|---|---|---|---|---|---|
| | | δiso (±0.2 ppm) | CQ (±0.2 MHz) | η (±0.1) | Iarea (±2%) | δiso (±0.5 ppm) | PQ (±0.5 MHz) |
| (2) | 1 | -5.2 | 1.0 | 0.8 | 48 | – | – |
| | 2 | -1.0 | 2.1 | 0.9 | 48 | – | – |
| (3) | 5 | 9.8[a] | – | – | 4 | – | – |
| | 1 | -5.0 | 1.1 | 0.8 | 37 | -5.2 | 1.1 |
| | 2 | -1.8 | 2.3 | 0.9 | 37 | -1.3 | 2.4 |
| | 3 | -3.7 | 1.6 | 0.8 | 9 | -3.4 | 1.6 |
| | 4 | 1.0 | 1.8 | 0 | 13 | – | – |
| | 5 | 9.6[a] | – | – | 4 | – | – |
| (4) | 1 | -5.1 | 1.1 | 0.8 | 37 | – | – |
| | 2 | -2.0 | 2.0 | 1.0 | 35 | – | – |
| | 3 | -3.1 | 1.6 | 0.8 | 11 | – | – |
| | 4 | 1.2 | 1.7 | 0 | 12 | – | – |
| | 5 | 9.3[a] | – | – | 5 | – | – |
| $P2_1ma$[b] | Na (a) | -1.5 | 2.1 | 0.9 | – | -1.5 | 2.4 |
| | Na (b) | -5.1 | 1.1 | 0.7 | – | -5.1 | 1.2 |
| Pbcm[b] | Na (a) | -0.5 | 2.1 | 0 | – | -0.5 | 2.1 |
| | Na (b) | -4.2 | 1.0 | 0.8 | – | -4.2 | 1.2 |

[a] Position of the peak maxima. [b] Extracted from ref. [23].

calculated using the equation:

$$\%\ of\ removal = \left[\frac{Co - Cf}{Co}\right] X100 \quad (3)$$

where Co and Cf represent the initial and final concentration of the dye respectively. As can be seen, in basic media the percentage of MB removal is considerably higher than in acidic media.

It is worth mentioning that the MB is a cationic molecule. With the increase in the pH of the medium, there is a change in the surface charges of the particles of the catalysts, becoming negatively charged [56], therefore the adsorption of the dye on the surface of the catalyst becomes more extensive, also increasing the molecule's photodegradation to a certain extent [56]. This result suggests that the mechanism of MB degradation by alkaline niobates occurs mainly on the surface of the materials, so their excitation by light, and the degradation of the dye molecule, can be described by the equations [57]:

$MNbO_3 + hv \rightarrow MNbO_3\ (h^+_{VB}) + MNbO_3\ (e^-_{CB})$, where M = Li or Na

$MNbO_3\ (h^+_{VB}) + MB \rightarrow MB^{+\bullet} + MNbO_3$

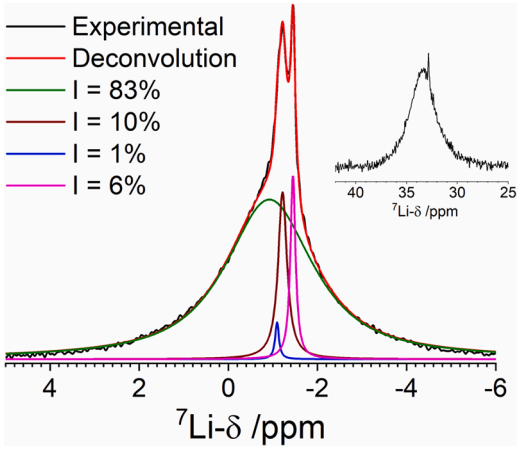


**Fig. 6.** Experimental (black curves) $^7$Li MAS NMR spectra for the $LiNbO_3$ sample. Coloured curves correspond to the spectral deconvolution into Gauss/Lorentz functions. The inset show the first order high-frequency spinning sideband for the experimental data.

**Table 5**
Parameters obtained from the deconvolution of the $^7$Li spectrum in Fig. 6 into Gauss/Lorentz functions. G/L is the Gauss/Lorentz fraction used for the fit and I is the intensity area for each component, taking into consideration the area of the corresponding spinning sidebands.

| Component | Pos (± 0.1 ppm) | Width (± 0.05 ppm) | G/L | I (±1%) |
|---|---|---|---|---|
| 1 | -0.9 | 2.36 | 0.3 | 83 |
| 2 | -1.2 | 0.24 | 0 | 10 |
| 3 | -1.1 | 0.10 | 0 | 1 |
| 4 | -1.5 | 0.14 | 0 | 6 |

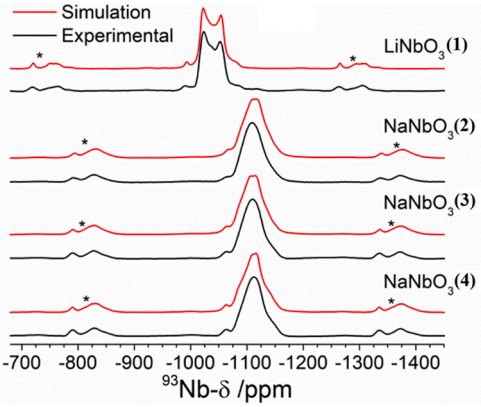


**Fig. 7.** Experimental (black curves) and simulated (red curves) $^{93}$Nb MAS NMR spectra for the investigated $LiNbO_3$ and $NaNbO_3$ compounds.

**Table 6**
Chemical shift anisotropy ($\Delta_{CS}$) was added to the simulations just to reproduce the first order spinning sidebands, the effect of this parameter in the spectral lineshape is minimum and it could not be accurately determined.

| Sample | $\delta_{iso}$ (±4 ppm) | $\Delta_{CS}$ (±50 ppm) | $C_Q$ (±1 MHz) | η (±0.1) | lb (±0.1 kHz) |
|---|---|---|---|---|---|
| $LiNbO_3$ (1) | -1005 | -90 | 22 | 0.1 | 1.0 |
| $NaNbO_3$ (2) | -1075 | -150 | 21 | 0.6 | 1.8 |
| $NaNbO_3$ (3) | -1078 | -150 | 21 | 0.6 | 2.0 |
| $NaNbO_3$ (4) | -1075 | -150 | 21 | 0.7 | 1.5 |

$$MNbO_3\ (h^+_{VB}) + H_2O \rightarrow OH^{\bullet} + H^+ + MNbO_3$$

Because the MB is light sensitive, the catalyst can also be excited directly:

$$MNbO_3 + MB^* \rightarrow MB^{+\bullet} + MNbO_3\ (e^-_{CB})$$

$$MNbO_3\ (e^-_{CB}) + O_2 \rightarrow MNbO_3 + O_2^{\bullet}$$

$$MNbO_3\ (e^-_{CB}) + O_2^{\bullet} + H^+ \rightarrow HO_2^- + MNbO_3$$

$$HO_2^- + H^+ \rightarrow H_2O_2$$

$$H_2O_2 + e^- \rightarrow OH^{\bullet} + OH^-$$

A higher concentration of $OH^-$ in these conditions might be the key factor that enhances the degradation process in an alkaline medium. This chemical group can react on the semiconductor surface with the valence band, and generate a greater amount of hydroxyl radicals ($OH^{\bullet}$) [56]. It can also be observed from the results shown in Fig. 8, that the variation of pH affects the photocatalytic activity of the $NaNbO_3$, compared to $LiNbO_3$. While $LiNbO_3$ removes approximately 42 and 48% at pH 1 and 12 respectively, $NaNbO_3$ removes approximately 59 and 87% under the same conditions. In addition, the results show that, regardless of pH, $NaNbO_3$ is a more efficient photocatalyst for MB than $LiNbO_3$.

The degradation kinetics was also investigated by varying the concentration of the dye as a function of time. It generally follows the mechanism of Langmuir – Hinshelwood [56]:

$$r = -\frac{dC}{dt} = \frac{kKC}{1+KC} \tag{4}$$

where r is the reagent degradation rate (mg/L min), C is the reagent concentration (mg/L), t is the radiation time, k is the reaction rate constant (mg/L min), and K is the reagent adsorption constant (L/mg). When C is too small, the equation can be simplified to:

$$\ln\left(\frac{C}{Co}\right) = kKt = K_{app}t \tag{5}$$

where $K_{app}$ is the first-order apparent rate constant, which is given by the slope of the graph of ln (C/Co) versus t, and Co is the initial reagent concentration. Fig. 9 shows a graph of ln (C/Co) versus time for the two niobates, at pH 1 and 12, Fig. 9a and 9b respectively.

These results follow the Langmuir-Hinshelwood kinetic behavior, as they presented correlation coefficients equal to 0.95 and 0.99 for $LiNbO_3$ and $NaNbO_3$, respectively, at pH 1, and 0.91 and 0.99 at pH 12. The apparent rate constant $K_{app}$, obtained from the graphs in Fig. 9, confirms what had been observed previously in the removal percentage graphs, that $NaNbO_3$ is more efficient in removing MB than $LiNbO_3$. The $K_{app}$ for the reaction of $NaNbO_3$ at pH 1 is 0.00716 $min^{-1}$ with an error of 2.22 × $10^{-4}$, whereas for $LiNbO_3$ it is 0.00271 $min^{-1}$ with an error of 1.86 × $10^{-4}$. At pH 12 the constants are 0.01569 $min^{-1}$ with an error of 5.3 × $10^{-4}$, and 0.00559 $min^{-1}$ with an error of 5.0 × $10^{-4}$, for $NaNbO_3$ and $LiNbO_3$, respectively. According to the literature, one of the factors that have made alkali metal niobates gain relative prominence in recent years, is their distorted octahedral structure, mainly $NbO_6$, which are active sites for photocatalysis in niobium compounds, being of crucial importance in the degradation of organic compounds [25]. From crystallography data, it is possible to observe that octahedron $NbO_6$ of $NaNbO_3$ ($P2_1ma$) is less ordered than the $LiNbO_3$ (R3c), displaying more distortions at the Nb(V) coordination. This may improve the catalytic activity of the sodium

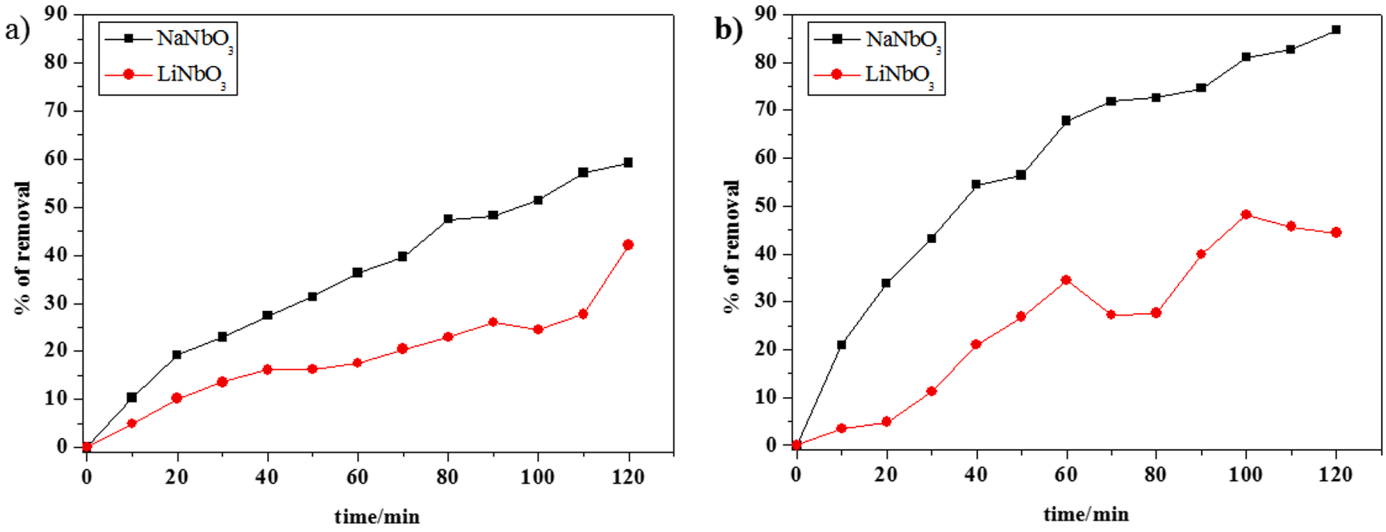


**Fig. 8.** Percentage of MB removal of photocatalytic test of samples (1) (red circles) and (2) (black squares), a) pH =1, and b) pH = 12.

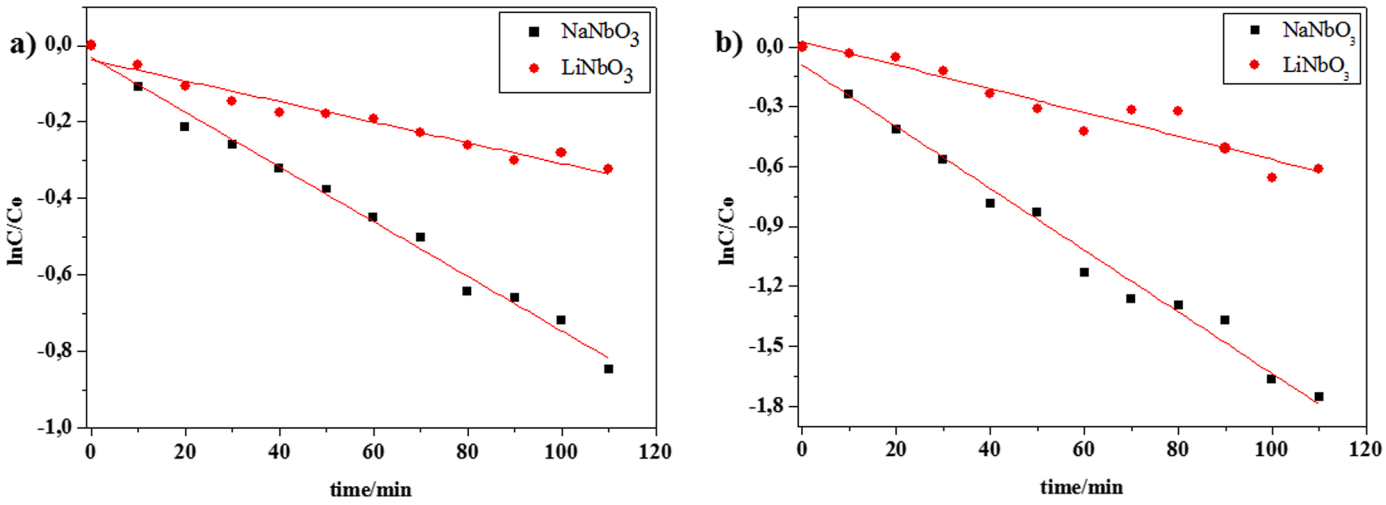


**Fig. 9.** ln (C/Co) versus t and fitted function to the pseudo first-order reaction kinetics of photocatalitic tests for samples (1) (red circles) and (2) (black squares), a) pH = 1, and b) pH = 12.

niobate in the degradation of MB. In addition, as demonstrated in the calculations of the Urbach energies, niobates synthesized by the method used in the present work, generate surface defects that normally improve the catalytic activity of the materials [58,59]. This is also a differential of the present work in comparison with others in the literature, where conventional synthetic approaches are employed, causing low compositional homogeneity, high sintering temperatures and large particle size, limiting their practical use in the industry photocatalysts [25]. Moreover, concerning the photocatalytic property of alkaline niobates, some authors attribute the activity to the Nb(V) 4d states relatively close to the minimum of the conduction band, which provide greater mobility for the photoinduced electrons ($e^-$), contributing to a good photocatalytic activity [25,60,61].

## 3. Conclusions

Nanoparticles of lithium and sodium niobates were successfully synthesized for the first time by microwave-assisted combustion. We observed that the amount of salt and counter-ion of the reactant can significantly change the crystalline and electronic structures and the microstructure of the products, indicating that this synthetic approach offers good control of the material properties. An orthorhombic structure was obtained for $NaNbO_3$ while $LiNbO_3$ displays a rhombohedral arrangement, as confirmed by powder XRD. $^{23}Na$ solid-state NMR results showed that the $NaNbO_3$ sample prepared with 1:1 Nb:NaCl molar ratio presents the $P2_1ma$ space group, while the samples prepared with NaCl in excess or with $NaNO_3$ salt (1:1 mol:mol) are both composed of a mixture of c.a. 86% P21ma and c.a. 14% distorted Pbcm phases. The nanoparticle size is influenced by the synthesis condition: the presence of the chloride anion or the salt in excess induces the production of smaller particles. The sample prepared with an excess of salt shows the largest bandgap, which denotes quantum confinement. The excess of alkali salt at the time of combustion provides a physical barrier to the growth of the particles. The Urbach energies of these samples are greater than 0.34 eV, indicating a considerable density of the structural distortions, as commonly found for nanostructured materials due to surface defects. The obtained lithium niobate and sodium niobate were used for photocatalytic degradation of methylene blue dye. Both $NaNbO_3$ and $LiNbO_3$ were able to induce the degradation of the target molecule. We also observed that these materials are stable and active over a wide range of pH (1 to 12). Therefore, the pH of the medium can be adjusted to increase the efficiency without compromising their chemical stability, making $NaNbO_3$ and $LiNbO_3$ versatile materials for the degradation of pollutants. Among the investigated materials, the $NaNbO_3$ was more efficient in all investigated conditions.

## Declaration of Competing Interest

The authors declare that they have no known competing financial interests or personal relationships that could have appeared to influence the work reported in this paper.

## Data availability

Data will be made available on request.

## Acknowledgements

The HRTEM and SEM images were obtained at the Microscopy Center of UFMG/Brazil. The authors acknowledges financial support from Fundação de Amparo à Pesquisa do Estado de Minas Gerais (Fapemig / Brazil) Universal APQ-01615–21. M. O. Jr acknowledges the National Council for Scientific and Technological (CNPq, grant n° 311069/2020–7).

## References

[1] J.P. Shi, X.L. Chen, C.C. Sun, F.H. Pang, H.Y. Chen, X.Y. Dong, X.J. Zhou, K. G. Wang, H.F. Zhou, Superior thermal and frequency stability and decent fatigue endurance of high energy storage properties in NaNbO3-based lead-free ceramics, Ceram. Int. 46 (2020) 25731–25737, https://doi.org/10.1016/j.ceramint.2020.07.050.

[2] G.F. Teixeira, E. Silva, A.Z. Simoes, E. Longo, M.A. Zaghete, Unveiling the correlation between structural order-disorder character and photoluminescence emissions of NaNbO3, Crystengcomm 19 (2017) 4378–4392, https://doi.org/10.1039/c7ce00218a.

[3] X.Y. Dong, X. Li, X.L. Chen, H.Y. Chen, C.C. Sun, J.P. Shi, F.H. Pang, H.F. Zhou, High energy storage density and power density achieved simultaneously in NaNbO3-based lead-free ceramics via antiferroelectricity enhancement, J. Materiomics 7 (2021) 629–639, https://doi.org/10.1016/j.jmat.2020.11.016.

[4] Y.F. Liu, W.F. Wang, C. Liu, C.C. Liu, J.K. Xu, Z.Y. Zhu, J.J. Yang, Y.Y. Wang, F. X. Jiang, Effects of inorganic salt NaNbO3 composite on the thermoelectric properties of tellurium nanorods thin slice, J. Alloys Compd. (2020) 849, https://doi.org/10.1016/j.jallcom.2020.156630.

[5] T. Runcevski, Rietveld refinement practical powder diffraction pattern analysis using TOPAS. By Robert E. Dinnebier, Andreas Leineweber and John S. O. Evans. De Gruyter, 2019. Pp. 331. Price (paperback) EUR 69.95, USD 80.99, GBP 63.50. ISBN 978-3-11-045621-9, e-ISBN (PDF) 978-3-11-046138-1, J. Appl. Crystallogr. 52 (2019) 1238–1239.

[6] A. Kaushalram, T.R. Yadunath, P.P. Das, G. Hegde, S. Talabattula, Ultra-broadband fabrication-tolerant mode division (de)multiplexer on thin film Lithium niobate, Opt. Commun. (2020) 475, https://doi.org/10.1016/j.optcom.2020.126251.

[7] C.Y. Shi, J. Yuan, X. Luo, S.X. Shi, S. Lu, P.F. Yuan, W.D. Xu, Z. Chen, H. Yu, Transmission characteristics of multi-structure bandgap for lithium niobate integrated photonic crystal and waveguide, Opt. Commun. (2020) 461, https://doi.org/10.1016/j.optcom.2019.125222.

[8] H.L. Song, X.F. Yu, X.L. Wang, A Low propagation loss planar waveguide structure fabricated on lithium niobate via low fluence argon-ion irradiation, Optik (Stuttg) (2020) 223, https://doi.org/10.1016/j.ijleo.2020.165435.

[9] D.D. Zhang, J.J. Qi, H.D. Ji, S. Li, L. Chen, T.B. Huang, C.K. Xu, X.M. Chen, W. Liu, Photocatalytic degradation of ofloxacin by perovskite-type NaNbO3 nanorods modified g-C3N4 heterojunction under simulated solar light: theoretical calculation, ofloxacin degradation pathways and toxicity evolution, Chem. Eng. J. (2020) 400, https://doi.org/10.1016/j.cej.2020.125918.

[10] G. Singh, M. Kumar, M. Singh, R. Vaish, Surface plasmon resonance triggered promising visible light photocatalysis of LiNbO3 ceramic supported Ag nanoparticles, J. Am. Ceramic Soc. 104 (2021) 1237–1246, https://doi.org/10.1111/jace.17538.

[11] S.S. Wang, Z. Wu, J. Chen, J.P. Ma, J.S. Ying, S.C. Cui, S.G. Yu, Y.M. Hu, J.H. Zhao, Y.M. Jia, Lead-free sodium niobate nanowires with strong piezo-catalysis for dye wastewater degradation, Ceram. Int. 45 (2019) 11703–11708, https://doi.org/10.1016/j.ceramint.2019.03.045.

[12] J. Yu, X.Q. Liu, Hydrothermal synthesis and characterization of LiNbO3 crystal, Mater. Lett. 61 (2007) 355–358, https://doi.org/10.1016/j.matlet.2006.04.087.

[13] A. El Bachiri, M. El Hasnaoui, A. Louardi, A. Narjis, F. Bennani, Structural and dielectric studies for the conduction mechanism analyses of lithium-niobate oxide ferroelectric ceramics, Physica B-Condensed Matter 571 (2019) 181–187, https://doi.org/10.1016/j.physb.2019.07.002.

[14] J.Y. Zubarev, S.H. Chang, C. Lin, N.A. Boldyrev, A.V. Pavlenko, A.V. Nazarenko, A. V. Nagaenko, Y.I. Yurasov, I.A. Verbenko, I.A. Parinov, et al., Phase states, microstructure and dielectric characteristics of solid solutions (1 - x)NaNbO3 - xCa(2)Nb(2)O(7) and (1 - x) NaNbO3 - xSr(2)Nb(2)O(7), Heliyon 6 (2020), https://doi.org/10.1016/j.heliyon.2020.e05197.

[15] R.F. Ali, B.D. Gates, Synthesis of lithium niobate nanocrystals with size focusing through an Ostwald ripening process, Chem. Mater. 30 (2018) 2028–2035, https://doi.org/10.1021/acs.chemmater.7b05282.

[16] R.F. Ali, M. Bilton, B.D. Gates, One-pot synthesis of sub-10nm LiNbO3 nanocrystals exhibiting a tunable optical second harmonic response, Nanoscale Adv. 1 (2019) 2268–2275, https://doi.org/10.1039/c8na00171e.

[17] Wang, Y.; Zhou, X.Y.; Chen, Z.; Cai, B.; Ye, Z.Z.; Gao, C.Y.; Huang, J.Y. Synthesis of cubic LiNbO3 nanoparticles and their application in vitro bioimaging. Appl. Phys. a-Mater. Sci. Process. 2014, 117, 2121–2126, doi:10.1007/s00339-014-8630-x.

[18] R. Rosa, P. Veronesi, C. Leonelli, A review on combustion synthesis intensification by means of microwave energy, Chem. Eng. Processing-Process Intensification 71 (2013) 2–18, https://doi.org/10.1016/j.cep.2013.02.007.

[19] K. Frikha, L. Limousy, J. Bouaziz, S. Bennici, K. Chaari, M. Jeguirim, Elaboration of alumina-based materials by solution combustion synthesis: a review, Comptes Rendus Chimie 22 (2019) 206–219, https://doi.org/10.1016/j.crci.2018.10.004.

[20] R. Abbas, K.D. Martinson, T.Y. Kiseleva, G.P. Markov, P.Y. Tyapkin, V.I. Popkov, Effect of fuel type on the solution combustion synthesis, structure, and magnetic properties of YIG nanocrystals, Mater. Today Commun. (2022) 32, https://doi.org/10.1016/j.mtcomm.2022.103866.

[21] X.D. Liu, Y.T. Zheng, X.Y. Su, Y.D. Yu, Y.C. Yuan, R.J. Wang, S.Y. Zhu, Y.L. Bai, G. B. Ying, Precipitation and sintering behaviour of non-stoichiometric MgAl2O4 solid solution powder prepared by combustion synthesis, Ceram. Int. 48 (2022) 26964–26972, https://doi.org/10.1016/j.ceramint.2022.06.008.

[22] S. Aydinyan, H. Kirakosyan, A. Sargsyan, O. Volobujeva, S. Kharatyan, Solution combustion synthesis of MnFeCoNiCu and (MnFeCoNiCu)3O4 high entropy materials and sintering thereof, Ceram. Int. 48 (2022) 20294–20305, https://doi.org/10.1016/j.ceramint.2022.03.310.

[23] K.E. Johnston, C.C. Tang, J.E. Parker, K.S. Knight, P. Lightfoot, S.E. Ashbrook, The polar phase of NaNbO3: a combined study by powder diffraction, solid-state NMR, and first-principles calculations, J. Am. Chem. Soc. 132 (2010) 8732–8746, https://doi.org/10.1021/ja101860r.

[24] Y. Yu, M. Gu, L. Zhang, T.B. Tang, Z.S. Li, T. Yu, Li-7 NMR study on surface ionic diffusion in nanocrystalline LiNbO3, Surface Rev. Lett. 14 (2007) 583–586, https://doi.org/10.1142/s0218625x07009888.

[25] J.L. Liu, I. Shakir, D.J. Kang, Single crystalline LiNb3O8 nanoflakes for efficient photocatalytic degradation of organic pollutants, RSC Adv. 4 (2014) 4917–4920, https://doi.org/10.1039/c3ra45520c.

[26] U. Farooq, R. Phul, S.M. Alshehri, J. Ahmed, T. Ahmad, Electrocatalytic and enhanced photocatalytic applications of sodium niobate nanoparticles developed by citrate precursor route, Sci. Rep. 9 (2019), https://doi.org/10.1038/s41598-019-40745-w.

[27] J.B. Xu, F. Zhang, B.Y. Sun, Y.G. Du, G.Q. Li, W.F. Zhang, Enhanced photocatalytic property of Cu doped sodium niobate, Int. J. Photoenergy (2015) 2015, https://doi.org/10.1155/2015/846121.

[28] S.R. Jain, K.C. Adiga, V.R.P. Verneker, A new approach to thermochemical calculations of condensed fuel-oxidizer mixtures, Combust. Flame 40 (1981) 71–79, https://doi.org/10.1016/0010-2180(81)90111-5.

[29] F. Nakagomi, S.E. Cerruti, M.R. de Freitas, E.S.F. Neto, F.V. de Andrade, G. O. Siqueira, Niobium pentoxide produced by a novel method microwave assisted combustion synthesis, Chem. Phys. Lett. 729 (2019) 37–41, https://doi.org/10.1016/j.cplett.2019.05.003.

[30] A. Medek, L. Frydman, Multiple-quantum magic-angle spinning NMR: a new technique for probing quadrupolar nuclei in solids, J. Braz. Chem. Soc. 10 (1999) 263–277.

[31] M. Bak, J.T. Rasmussen, N.C. Nielsen, SIMPSON: a general simulation program for solid-state NMR spectroscopy, J. Magnetic Resonance 147 (2000) 296–330, https://doi.org/10.1006/jmre.2000.2179.

[32] Wachtler, M.; Schweitzer, A.; Gutmann, T.; Breitzke, H.; Buntkowsky, G. Efficient analysis of V-51 solid-state MAS NMR spectra using genetic algorithms. Solid State Nuclear Magnetic Resonance 2009, 35, 37–48, doi:10.1016/j.ssnmr.2008.11.003.

[33] M. Bak, N.C. Nielsen, REPULSION, a novel approach to efficient powder averaging in solid-state NMR, J. Magnetic Resonance 125 (1997) 132–139, https://doi.org/10.1006/jmre.1996.1087.

[34] B.M. Meyer, N. Leifer, S. Sakamoto, S.G. Greenbaum, C.P. Grey, High field multinuclear NMR investigation of the SEI layer in lithium rechargeable batteries, Electrochem. Solid State Lett. 8 (2005) A145–A148, https://doi.org/10.1149/1.1854117.

[35] S. Gates-Rector, T. Blanton, The powder diffraction file: a quality materials characterization database, Powder Diffr. 34 (2019) 352–360, https://doi.org/10.1017/s0885715619000812.

[36] Y. Shiratori, A. Magrez, J. Dornseiffer, F.H. Haegel, C. Pithan, R. Waser, Polymorphism in micro-, submicro-, and nanocrystalline NaNbO3, J. Phys. Chem. B 109 (2005) 20122–20130, https://doi.org/10.1021/jp052974p.

[37] J. Koruza, P. Groszewicz, H. Breitzke, G. Buntkowsky, T. Rojac, B. Malic, Grain-size-induced ferroelectricity in NaNbO3, Acta Mater. 126 (2017) 77–85, https://doi.org/10.1016/j.actamat.2016.12.049.

[38] K. Santra, P. Chatterjee, S.P. Sen Gupta, Voigt modelling of size-strain analysis: application to alpha-Al2O3 prepared by combustion technique, Bullet. Mater. Sci. 25 (2002) 251–257, https://doi.org/10.1007/bf02711163.

[39] G.K. Williamson, W.H. Hall, X-ray line broadening from filed aluminium and wolfram, Acta Metallurgica 1 (1953) 22–31, https://doi.org/10.1016/0001-6160(53)90006-6.

[40] J. Tauc, A. Menth, States in the gap, J. Non Cryst. Solids 8-10 (1972) 569–585, https://doi.org/10.1016/0022-3093(72)90194-9.

[41] C. Thierfelder, S. Sanna, A. Schindlmayr, W.G. Schmidt, Do we know the band gap of lithium niobate? Physica Status Solidi C: Current Topics in Solid State Phys. 7 (2) (2010) 362–365, https://doi.org/10.1002/pssc.200982473. VolNo7.

[42] E. Grabowska, Selected perovskite oxides: characterization, preparation and photocatalytic properties-A review, Appl. Catal. B-Environ. 186 (2016) 97–126, https://doi.org/10.1016/j.apcatb.2015.12.035.

[43] P. Li, H. Abe, J.H. Ye, Band-gap engineering of NaNbO3 for photocatalytic H-2 evolution with visible light, Int. J. Photoenergy (2014) 2014, https://doi.org/10.1155/2014/380421.

[44] G. Gouget, M.M. Duttine, E. Durand, A. Villesuzanne, V. Rodriguez, F. Adamietz, T. Le Mercier, M.D. Braida, A. Demourgues, Isolating the two room-temperature polymorphs of NaNbO3: structural features, optical band gap, and reactivity, Acs Appl. Electron. Mater. 1 (2019) 513–522, https://doi.org/10.1021/acsaelm.8b00125.

[45] R.C. Rai, Analysis of the Urbach tails in absorption spectra of undoped ZnO thin films, J. Appl. Phys. (2013) 113, https://doi.org/10.1063/1.4801900.

[46] A. Kumar, R. Kumar, N. Verma, A.V. Anupama, H.K. Choudhary, R. Philip, B. Sahoo, Effect of the band gap and the defect states present within band gap on the non-linear optical absorption behaviour of yttrium aluminium iron garnets, Opt. Mater. (Amst) 108 (2020), https://doi.org/10.1016/j.optmat.2020.110163.

[47] R. Bhatt, I. Bhaumik, S. Ganesamoorthy, A.K. Karnal, M.K. Swami, H.S. Patel, P. K. Gupta, Urbach tail and bandgap analysis in near stoichiometric LiNbO3 crystals, Physica Status Solidi a-App. Mater. Sci. 209 (2012) 176–180, https://doi.org/10.1002/pssa.201127361.

[48] P. Bindu, S. Thomas, Optical properties of ZnO nanoparticles synthesised from a polysaccharide and ZnCl2, Acta Physica Polonica A 131 (2017) 1474–1478, https://doi.org/10.12693/APhysPolA.131.1474.

[49] M. Wilkening, D. Bork, S. Indris, P. Heitjans, Diffusion in amorphous LiNbO3 studied by Li-7 NMR comparison with the nano- and microcrystalline material, Phys. Chem. Chem. Phys. 4 (2002) 3246–3251, https://doi.org/10.1039/b201193j.

[50] Y. Xia, N. Machida, X.H. Wu, C. Lakeman, L. vanWullen, F. Lange, C. Levi, H. Eckert, Li-7 and Li-6 solid-state NMR studies of structure and dynamics in LiNbO3-WO3 solid solutions, J. Phys. Chem. B 101 (1997) 9180–9187, https://doi.org/10.1021/jp971751z.

[51] K.E. Johnston, J.M. Griffin, R.I. Walton, D.M. Dawson, P. Lightfoot, S.E. Ashbrook, Nb-93 NMR and DFT investigation of the polymorphs of NaNbO3, Phys. Chem. Chem. Phys. 13 (2011) 7565–7576, https://doi.org/10.1039/c1cp20258h.

[52] R. Kind, H. Graniche, B. Derighet, F. Waldner, E. Brun, NMR OF 93NB in ferroelectric LINBO3, Solid State Commun. 6 (1968), https://doi.org/10.1016/0038-1098(68)90050-1, 439-&.

[53] S. Prasad, P. Zhao, J. Huang, J.J. Fitzgerald, J.S. Shore, Niobium-93 MQMAS NMR spectroscopic study of alkali and lead niobates, Solid State Nucl. Magn. Reson. 19 (2001) 45–62, https://doi.org/10.1006/snmr.2000.0022.

[54] J. Davis, D. Tinet, J.J. Fripiat, J.M. Amarilla, B. Casal, E. Ruizhitzky, V-51 and NB-93 high-resolution NMR-study of NBVO5, J. Mater. Res. 6 (1991) 393–400, https://doi.org/10.1557/jmr.1991.0393.

[55] O.B. Lapina, D.F. Khabibulin, K.V. Romanenko, Z.H. Gan, M.G. Zuev, V. N. Krasil'nikov, V.E. Fedorov, Nb-93 NMR chemical shift scale for niobia systems, Solid State Nucl. Magn. Reson. 28 (2005) 204–224, https://doi.org/10.1016/j.ssnmr.2005.09.003.

[56] I. Kazeminezhad, A. Sadollahkhani, Influence of pH on the photocatalytic activity of ZnO nanoparticles, J. Mater. Sci.-Mater. Electron. 27 (2016) 4206–4215, https://doi.org/10.1007/s10854-016-4284-0.

[57] Y.J.O. Asencios, M.V. Quijo, F.C.F. Marcos, A.E. Nogueira, R.R. Rocca, E.M. Assaf, Photocatalytic activity of Nb heterostructure (NaNbO3/Na2Nb4O11) and Nb/clay

materials in the degradation of organic compounds, Solar Energy 194 (2019) 37–46, https://doi.org/10.1016/j.solener.2019.10.005.
[58] M. Sun, L. Yu, F. Ye, G.Q. Diao, Q. Yu, Y.Y. Zheng, J.Y. Piquemal, Rapid synthesis of cryptomelane-type manganese oxide under ultrasonic process, Mater. Lett. 65 (2011) 3184–3186, https://doi.org/10.1016/j.matlet.2011.06.108.
[59] R. Ianos, R. Lazau, R.C. Boruntea, Solution combustion synthesis of bluish-green BaAl2O4: eu2+, Dy3+ phosphors, Ceram. Int. 41 (2015) 3186–3190, https://doi.org/10.1016/j.ceramint.2014.10.171.
[60] V.V. Atuchin, I.E. Kalabin, V.G. Kesler, N.V. Pervukhina, Nb 3d and O 1s core levels and chemical bonding in niobates, J. Electron. Spectros. Relat. Phenomena 142 (2005) 129–134, https://doi.org/10.1016/j.elspec.2004.10.003.
[61] E.M. Sabio, M.F. Chi, N.D. Browning, F.E. Osterloh, Charge separation in a niobate nanosheet photocatalyst studied with photochemical labeling, Langmuir 26 (2010) 7254–7261, https://doi.org/10.1021/la904377f.